Electrochimica Acta 322 (2019) 134771

Contents lists available at ScienceDirect

Electrochimica Acta

journal homepage: www.elsevier.com/locate/electacta

Porous nickel oxide microsphere and $Ti_3C_2T_x$ hybrid derived from metal-organic framework for battery-type supercapacitor electrode and non-enzymatic H_2O_2 sensor

Rajendran Ramachandran [a, b, c], Changhui Zhao [b], Muniyandi Rajkumar [d], Krishnamoorthy Rajavel [e], Pengli Zhu [e], Wenlu Xuan [b], Zong-Xiang Xu [c, **], Fei Wang [b, f, *]

[a] SUSTech Academy for Advanced Interdisciplinary Studies, Southern University of Science and Technology, Shenzhen, 518055, China
[b] School of Microelectronics, Southern University of Science and Technology, Shenzhen, 518055, China
[c] Department of Chemistry, Southern University of Science and Technology, Shenzhen, 518055, China
[d] School of Chemistry and Environmental Engineering, Shenzhen University, Shenzhen, 518055, China
[e] Shenzhen Institute of Advanced Electronic Materials - Shenzhen Fundamental Research Institutions, Shenzhen Institutes of Advanced Technology, Chinese Academy of Sciences, Shenzhen, 518055, China
[f] GaN Device Engineering Technology Research Center of Guangdong, Southern University of Science and Technology, Shenzhen, 518055, China

ARTICLE INFO

Article history:
Received 11 July 2019
Received in revised form
11 August 2019
Accepted 26 August 2019
Available online 29 August 2019

Keywords:
$NiO/Ti_3C_2T_x$
Cyclic voltammetry
Differential pulse voltammetry
Hydrogen peroxide
Supercapacitor

ABSTRACT

The porous structure of three-dimensional NiO microspheres on titanium carbide ($NiO/Ti_3C_2T_x$) is prepared by calcination of Ni-MOF/$Ti_3C_2T_x$ in the air. The crystalline structure and morphology of the obtained hybrid are characterized with various tools such as X-ray photoelectron spectroscopy and X-ray diffraction, scanning electron microscope, transmission electron microscope, and Brunauer-Emmett-Teller surface analyzer techniques. As-prepared $NiO/Ti_3C_2T_x$ hybrid is used for two noteworthy applications in electrochemistry like supercapacitor and non-enzymatic hydrogen peroxide (H_2O_2) sensor. $NiO/Ti_3C_2T_x$ electrode exhibited an enhanced specific capacity of 630.9C g^{-1} at a current density of 1 A g^{-1} in comparison to pure NiO (376.8C g^{-1}). Furthermore, the H_2O_2 sensing performance of the $NiO/Ti_3C_2T_x$ modified glassy carbon electrode is evaluated in 0.5 M of NaOH solution and the electrode showed a low detection limit of 0.34 μM with a wider range of linear response 10 μM to 4.5 mM. The higher specific surface area and porosity of $NiO/Ti_3C_2T_x$ allow more electro-active site for electrochemical redox reactions in the direction of H_2O_2 sensing and supercapacitor. Moreover, $Ti_3C_2T_x$ prevents from fouling in 3D porous network and leaching effect, and beneficial for easy access of electrolyte ions and efficient electron transport to the electrode surface resulted in improved electrochemical applications.

1. Introduction

In the past several years, metal-organic frameworks (MOFs) and their derived materials with high surface area and stable porous architectures have been received considerable attention in the wide range of potential applications [1]. The ultra-high porosity, and pore size tenability make them as potential material for applications not only for gas storage, separation, and catalysis, but also for electrochemical fields such as supercapacitor, lithium−ion batteries and electrochemical sensors because of their active metal sites, and diversity of composition and structure [2]. Like conventional inorganic materials, MOFs contain redox-active metal centers (Fe, Co, Ni, Mn, etc.), which are of appropriate interest for delivering electrochemical activity. Besides, MOFs have been confirmed to be flexible templates for the synthesis of porous micro/nanomaterials such as metal oxides, metal sulfides, carbon materials with a hierarchical structure, inheritance morphology and high specific surface area by controlling pyrolysis process, the research direction has been turned to produce MOF derived materials for various potential applications [3,4]. Till date, numerous metal oxides including CuO, Co_3O_4, Fe_2O_3, ZnO, CeO_2, NiO, etc have

* Corresponding author. School of Microelectronics, Southern University of Science and Technology, Shenzhen, 518055, China.
** Corresponding author. Department of Chemistry, Southern University of Science and Technology, Shenzhen, 518055, China.
E-mail addresses: xu.zx@sustech.edu.cn (Z.-X. Xu), wangf@sustech.edu.cn (F. Wang).

https://doi.org/10.1016/j.electacta.2019.134771
0013-4686/

been synthesized directly from MOF for various applications including supercapacitors and electrochemical sensors [2]. Typically, the metal oxides nanostructures derived from MOF possess a porous structure with the high surface area, which is significant in achieving better electrochemical performance. Among various metal oxides, Nickel oxide (NiO) with thermally stable semiconducting properties has gained much research interest due to their excellent redox behavior and higher theoretical capacitance ($2584\ F\ g^{-1}$) [5]. Moreover, the existence of the interchangeable oxidation states in NiO allows fast intercalate/deintercalate of electrolyte ions resulting in high specific capacity during electrochemical redox activities [6]. However, the difficulty of poor electron transportation of NiO through the electrochemical redox reaction process is limited to its electrochemical applications.

Owing to possess excellent electrical conductivity and accomplishing highly effective electrochemical signal transduction is an essential path of metal oxides, introducing some functional materials such as graphene, CNT, etc can be an effective way which has excellent electronic conductivity and make MOF derived metal oxides more stable [7,8]. More recently, titanium carbide (MXene) is an emerging 2D material with excellent electrical conductivity, which could deliver better electrochemical performance due to its extremely reversible redox reactions in the hydrophilic surfaces and metallic electrical conductivity [9]. The general composition formula of MXene is $M_{n+1}X_nT_x$ where M is an early transition metal, X is Carbon and/or Nitrogen, and $n = 1$, 2, 3 and T_x represents functional groups such as −OH, and −F. Among various MXenes, $Ti_3C_2T_x$ is the most investigated and the abundant functional group (T_x) in $Ti_3C_2T_x$ can exhibit hydrophilic behavior which enhances the redox activities during electrochemical reactions [10,11]. Considering these factors, it is noteworthy to investigate the preparation of novel NiO/$Ti_3C_2T_x$ hybrid from MOF for electrochemical applications such as supercapacitor and hydrogen peroxide (H_2O_2) sensor.

The worldwide research is continuously discovering novel materials in addition to enhancing features like electrical and electrocatalytic properties to fabricate highly efficient electronic devices; which includes electrochemical capacitors [12], batteries [13], and sensors [14]. Particularly, significant effort has been made on electrode modification with highly electrocatalytic material and development of the new material with low cost and high energy density for the detection of biomolecules, compounds, and high-performance energy storage applications [15]. For instance, supercapacitor with high energy density has been widely investigated as the potential device for electrical energy storage application than lithium-ion batteries. However, the commercially available supercapacitors are hindered by their lower energy density and low rate capability. Therefore, a primary target is to synthesis and design a stable electrode material with the high surface area and greater electrochemical reversibility [16,17].

In addition, the electrochemical sensors are substantially essential for the detections of biomolecules such as hydrogen peroxide, glucose, dopamine, etc in the bio-medical applications [18]. Among different analytes, hydrogen peroxide (H_2O_2) is a universal oxidant that plays an essential role in various fields such as pharmaceutical, environmental, food, chemical and biochemical industries [19]. Thus, rapid and accurate technology of H_2O_2 detection is of great importance, which has attracted much research interest. Among different techniques such as spectrophotometry [20], tritimetry [21], chemiluminescence [22] and electrochemical [23], the electrochemical method for H_2O_2 detection have drawn considerable attention for its practical merits such as accuracy, low cost, high sensitivity, simplicity and time savings [24]. There are generally two types of sensors, naming as enzyme and non-enzyme based sensors. Although enzyme based H_2O_2 sensor is capable of detecting a lower concentration of H_2O_2 with good selectivity, they are suffering from drawbacks such as instability and high cost expensive of enzymes. To overcome these drawbacks, many effects have been made for fabricating non-enzymatic sensors with various materials [25,26]. Till now, various novel materials including carbon materials like mesoporous carbon, carbon nanotube, graphene, and their composites, metal oxides, conducting polymers have been explored for the development of supercapacitors and electrochemical H_2O_2 sensors [27–29]. However, achieving a higher performance of supercapacitor and a boarder range together with the lowest detection limit of H_2O_2 detection on modified electrodes are a challenging task yet. Considering the facts as mentioned above, the development of the novel electrode material is a primary task, and it would be a favor for improving electrochemical characteristics of supercapacitor and H_2O_2 sensor. To the best of our knowledge, there is no literature yet about the synthesis of NiO/$Ti_3C_2T_x$ hybrid from MOF precursor for non-enzymatic H_2O_2 detection and supercapacitor electrode material.

In this work, we report a simple preparation of three dimensional porous NiO microsphere with $Ti_3C_2T_x$ architecture by calcining Ni-MOF/$Ti_3C_2T_x$ hybrid. The obtained NiO/$Ti_3C_2T_x$ hybrid possesses a high surface area ($72.019\ m^2\ g^{-1}$), which could improve the H_2O_2 detection and capacity performance by increased ion-accessible at the electrode/electrolyte interfaces. The maximum specific capacity of $630.9C\ g^{-1}$ reported for NiO/$Ti_3C_2T_x$ electrode, which was almost 1.6 times higher than that of pure NiO. Furthermore, the NiO/$Ti_3C_2T_x$ modified glassy-carbon electrode is exhibited an excellent non-enzymatic sensor towards H_2O_2 detection with the wider range of concentration (10 μM−4.5 mM) and a lower detection limit of 0.34 μM.

2. Experimental method

2.1. Materials

Nickel (II) nitrate hexahydrate ($Ni(NO_3)_2{\cdot}6H_2O$), 1,3,5-tricarboxylic acid (H_3BTC), *N*,*N*-dimethylformamide ($(CH_3)_2NCH$), Potassium Hydroxide (KOH), Hydrogen peroxide (H_2O_2) were purchased from Sigma-Aldrich. Hydrofluoric acid (HF) was procured from Aladdin chemical reagent, China. All the solutions were prepared using Milli-Q water (pH 7.2).

2.2. Synthesis of NiO/$Ti_3C_2T_x$ hybrid

NiO/$Ti_3C_2T_x$ hybrid was prepared by a two-step process, which includes solvothermal preparation of Ni-MOF/$Ti_3C_2T_x$ followed by annealing treatment as shown in Scheme 1. $Ti_3C_2T_x$ was prepared through HF treatment of MAX powder (Ti_3AlC_2) according to our previous report [11]. The process of Ni-MOF/$Ti_3C_2T_x$ hybrid involves that initially 20 mg of $Ti_3C_2T_x$ powder in 48 mL of DMF solution was sonicated for half an hour after that 0.9 g of H_3BTC was added into the former solution and stirred for 10 min. Later, 1.8 g of $Ni(NO_3)_2{\cdot}6H_2O$ was added and continued stirring for another 10 min. Then the mixture was transferred into a Teflon-lined stainless steel autoclave (70 mL capacity) and sealed tightly. Then the autoclave was kept in a hot air oven and heated to 120 °C for 24 h (Step-I). After the natural cooling to room temperature, the obtained precipitate was washed continuously with DMF and ethanol, and the resultant product was dried at 70 °C for 12 h in a vacuum oven. The prepared sample was named as Ni-MOF/$Ti_3C_2T_x$. The synthesis of pure Ni-MOF was similar to that illustrated above without $Ti_3C_2T_x$, and the sample was named as Ni-MOF.

Then, the NiO/$Ti_3C_2T_x$ hybrid was prepared by annealing of Ni-MOF/$Ti_3C_2T_x$ powder in air at 350 °C for 2 h at a heating rate of 2 °C/

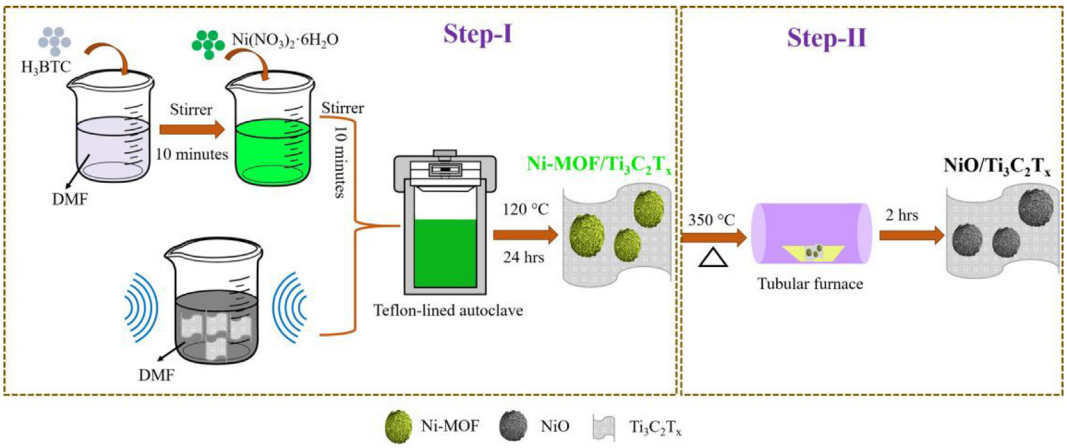

Scheme. 1. Schematic representation of the NiO/$Ti_3C_2T_x$ hybrid preparation process.

min (Step-II). Similarly, pure NiO was synthesized with bare Ni-MOF powder.

2.3. Materials characterization

X-ray diffraction (XRD) pattern of the synthesized samples was analyzed by Rigaku Smartlab with Cu-Kα radiation ($\lambda = 1.540$ Å). The morphologies and the structures of the samples were observed with a scanning electron microscope (SEM, Zeiss Merlin) and transmission electron microscope (TEM, Tecnai F30). The surface area and porosity of the samples were measured with BET ASAP 2020. The surface elements and their chemical states of the sample were identified by X-ray photoelectron spectroscopy (XPS, ESCALB 250Xi) with Mg K radiation.

2.4. Electrochemical measurements

The electrochemical properties of supercapacitor and H_2O_2 sensing were carried out in an electrochemical analyzer (CHI 660 E workstation). Ag/AgCl and Pt wire were used as reference and counter electrode, respectively. Cyclic voltammetry (CV), galvanostatic charge-discharge (GCD) and electrochemical impedance spectroscopy (EIS) were conducted in 3 M KOH electrolyte to find the redox activities of the active material towards supercapacitor. The working electrode of the supercapacitor was fabricated thorough slurry-coated technique. The slurry was prepared as follows: In brief, the active material, the conductive agent (carbon block) and the Nafion solution were mixed with a weight ratio of 80:15:5 along with a few drops of ethanol. Afterward, the suspending slurry solution was coated on Ni foam electrodes. Then the electrode was dried at 80 °C for 12 h. The total mass of the active material of the electrode was about 2 ± 0.1 mg cm^{-2}, and the coated area was about 1 cm × 1 cm.

2.5. Preparation of modified electrodes for H_2O_2 sensor

Typically, a glassy-carbon electrode was cleaned by polishing the electrode surface with alumina powder (0.05 μm) followed by sonicating in distilled water and ethanol for 10 minutues and allowed to dry in room temperature. A slurry was prepared by sonicating 5 mg of the sample (NiO, NiO/$Ti_3C_2T_x$) in 5 mL of ethanol for 30 min. After that, 6 μL of the above solution was drop casted on the polished electrode surface by using a micropipette and dried at room temperature. 0.5 M of NaOH solution was used as an electrolyte. H_2O_2 sensing performance was analyzed using Differential pulse voltammetry (DPV) technique.

3. Results and discussion

3.1. Material characterization

The XRD spectrum of exfoliated $Ti_3C_2T_x$ powder from Ti_3AlC_2 (MAX) phase is given in Fig. 1(b). It can be seen that major peaks of MAX is disappeared and the dominance of peaks at 8.49°, 18.54°, 26.61°, 27.71°, 34.30°, 43.48°, 52.40°, 57.49°, 60.60°, and 69.29° correspond to exfoliated $Ti_3C_2T_x$ layers structures which are matches with previous reports of quality MXene [10]. The crystallinity and the crystal phase of prepared bare NiO and NiO/$Ti_3C_2T_x$ hybrid from Ni-MOF were evaluated from XRD, as shown in Fig. 1 (b). The diffractions peaks at 37.1°, 43.3°, 62.8°, 75.7° and 79.4° corresponds to (111), (200), (220), (311) and (222) planes of face-centered cubic crystalline phase of NiO nanostructure correlated with previous reports and standard JCPDS 47−1049 [30]. The peak position corresponds to Ni-MOF is reorganized into NiO nanostructures after heat treatment confirms the effective conversion of Ni-MOF (Fig. 1(a)) into a crystalline phase of NiO.

After the addition of $Ti_3C_2T_x$ into NiO, the dominance of NiO peaks along with additional peaks of $Ti_3C_2T_x$ at 9.7°, 25.4°, 44.6° and 51.7° (indicated as * in Fig. 1(b)), confirms the NiO/$Ti_3C_2T_x$ hybrid formation. Interestingly, the diffraction peaks at 25.4° and 51.7° were shifted to a lower degree than that of pure $Ti_3C_2T_x$ (27.9 and 52.4°), which indicates that the attached NiO on $Ti_3C_2T_x$ sheets can prevent aggregation of MXene sheets [31]. The less diffraction intensity feature for MXene in NiO/$Ti_3C_2T_x$ hybrids can be attributed to the following reasons: (1) The lower weight percentage of $Ti_3C_2T_x$ in NiO might be reduced the intensity of $Ti_3C_2T_x$. (2) As the result of better crystallinity of nickel oxide in the composite, the diffraction peaks of $Ti_3C_2T_x$ was weakened. Thus minor diffraction peaks of $Ti_3C_2T_x$ remarked in the composite [32].

The N_2 adsorption-desorption isotherms at 77.4 K and Barrett-Joyner-Halenda (BJH) pore size distribution curves are shown in Fig. 1 (c) and (d), respectively, to determine the specific surface area and porosity properties of the as-prepared products. The isotherms are classified as a type-IV behavior with a distinct hysteresis loop type H3 in the range of ca. 0.8−1.0 P/P_o, indicating the mesoporous property of NiO [33]. Besides, the high adsorption and the sharp climbing peak observed at the high-pressure region indicates the presence of large mesoporous characteristics in NiO/$Ti_3C_2T_x$ hybrid, which could certainly attribute to the voids between the nanoplates in NiO microsphere [34]. The measured BET surface area of NiO and

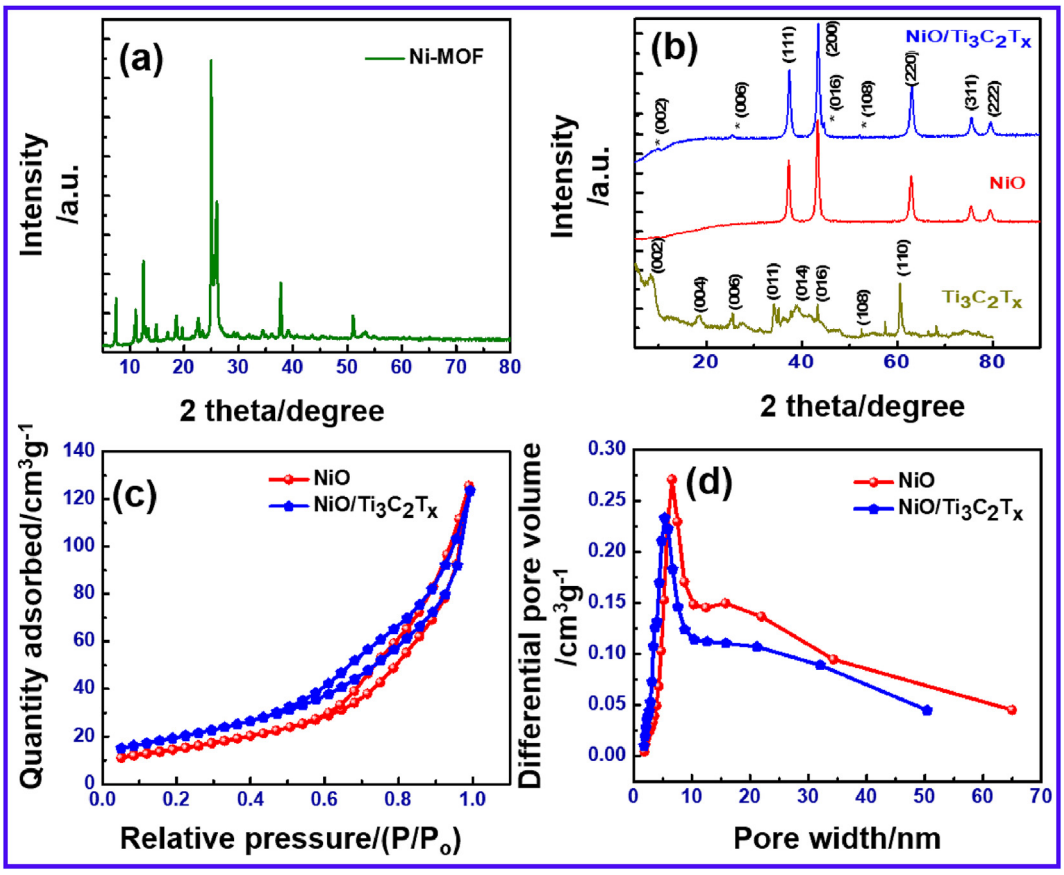

Fig. 1. (a, b) Powder X-ray diffraction patterns of bare Ni-MOF, $Ti_3C_2T_x$, NiO and NiO/$Ti_3C_2T_x$ hybrid. (c) N_2 adsorption-desorption isotherms (d) Barrett-Joyner-Halenda pore size distribution curves.

NiO/$Ti_3C_2T_x$ about 54.02 and 72.02 $m^2 g^{-1}$, respectively. The increased specific surface area suggests that the incorporation of $Ti_3C_2T_x$ sheets can effectively enhance the mesoporous structure as the result of interlayer voids (indicated in Fig. 2 f) and can maximize the accessibility of NiO. In addition, the mesoporous feature of prepared NiO/$Ti_3C_2T_x$ hybrid confirmed from BJH pore size distribution curve as shown in Fig. 1(d). It is observed that the hybrid shows the peak centered at around 5.2 nm and larger pore size (10–20 nm). Such porosity and higher specific surface area of NiO/$Ti_3C_2T_x$ allows more electro-active site for H_2O_2 sensing and would be beneficial for easy access of electrolyte ions and efficient electron transport to the electrode surface resulting in improved electrochemical performance.

The morphology of the samples is an essential factor for electrochemical redox reactions, as-prepared NiO and hybrid were characterized by SEM analysis as shown in Fig. 2. Fig. S1 demonstrates the two-dimensional layer structure of bare $Ti_3C_2T_x$. It can be seen that the as-obtained NiO reveals three-dimensional flower-like hierarchically porous microspheres architecture with numerous nanoplatelets or sheets as building blocks (Fig. 2 a-c). The measured average diameter of the microspheres is about ~4 μm. The fine porous structure of NiO is friendly to the fast electrolyte ion diffusion, which is profitable for better redox reactions. Furthermore, the auspicious decoration of NiO on $Ti_3C_2T_x$ sheets was verified by Fig. 2(d–f). The MXene sheets are effectively linked with the NiO microspheres, which can benefit electron transportation and increase the electrochemical active sites [35]. In addition, the voids in stacked $Ti_3C_2T_x$ layers (mentioned in Fig. 2(f)) enhance the insertion and extraction of electrolyte ions in the electrode/electrolyte interface during the electrochemical reactions. To further explore the microscopic morphology of the as-prepared active materials, high-resolution transmission electron microscope (HRTEM) analysis was conducted, and the images are shown in Fig. 3. From Fig. 3(a), it can be observed that the NiO microspheres were assembled with an approximate diameter of 4 μm along with densely tiny sheets architecture, which is consistent with previous SEM analysis. The hybrid structure of NiO/$Ti_3C_2T_x$ (Fig. 3(d–f)) clearly showed the attachment of MXene sheet on NiO, which would play a vital role in the electrical conductivity during the redox reaction. The corresponding selected area electron diffraction (SAED) pattern (inset in Fig. 3(f)) exhibited well diffraction rings that can be indexed towards the (111), (200), (220), (311) and (222) lattice planes of polycrystalline NiO. Besides, some of the additional weaker diffraction rings have been observed which might be attributed to the diffraction of $Ti_3C_2T_x$. Obviously, the combined benefits associated with NiO decorated $Ti_3C_2T_x$, and the presence of MXene sheets would contribute much to the electrochemical utilization and rate capability of NiO/$Ti_3C_2T_x$ hybrids.

The surface chemical composition and valence state of the elements in NiO and NiO/$Ti_3C_2T_x$ hybrid were further analyzed by high-resolution XPS. As depicted in full survey spectra (Fig. 4 (a)), bare NiO and NiO/$Ti_3C_2T_x$ reveal the presence of Ni and O elements which further confirm the formation of NiO structure from MOF. In addition, the existence of new peak around at ~450 eV (indicated as arrow mark in Fig. 4 a (ii)), which proves the hybrid of NiO/$Ti_3C_2T_x$ formation. As the evidence of Fig. 4 c, the deconvolution of Ti 2p spectrum consists of Ti $2p_{3/2}$ and Ti $2p_{1/2}$ core level with double

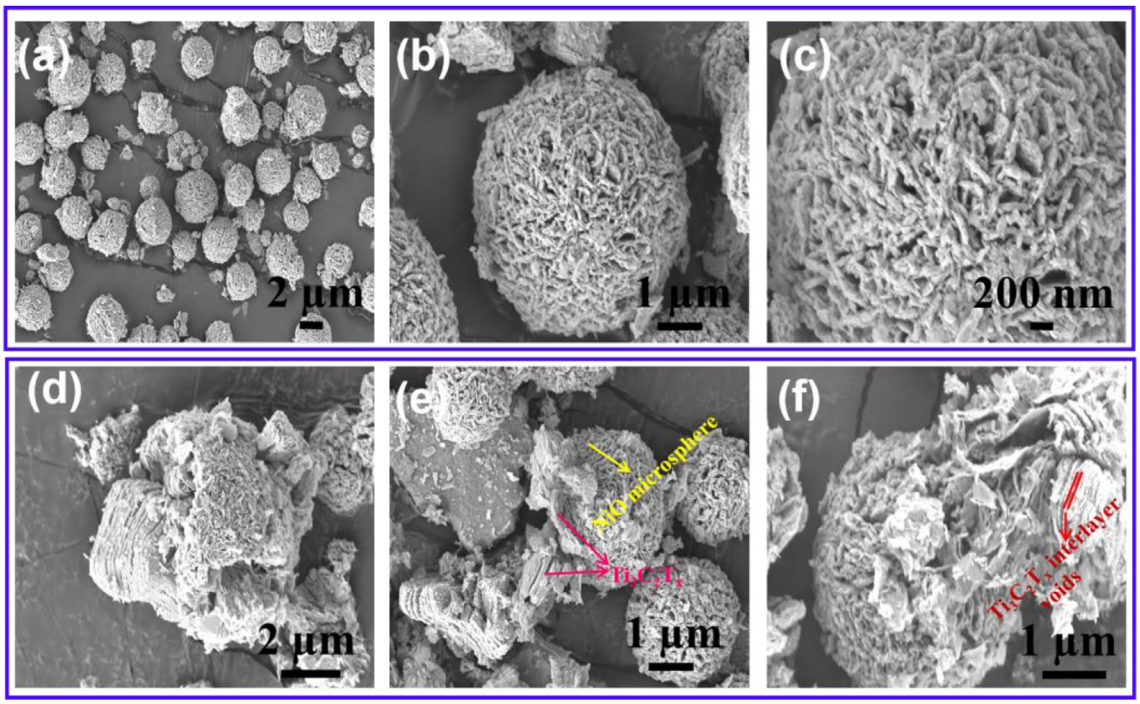

Fig. 2. SEM images of (a–c) NiO and (d–f) NiO/$Ti_3C_2T_x$ hybrid.

peak features and a fixed area ratio of 2:1, which is consistent with the previous report [36]. The peak located at 460.1 eV and 463.9 eV corresponds to Ti–C and Ti–C–Ti bonds of the core in Ti $2p_{3/2}$ and Ti $2p_{1/2}$, respectively [37,38]. Also, the other two peaks at 457.8 and 462.8 eV are associated with the unique bonds of Ti–O on the surface of $Ti_3C_2T_x$ [39], validating that the slight oxidation process of $Ti_3C_2T_x$ sheets during annealing. The C 1s peaks at 284.6, 286.2 and 288.3 eV are assigned to the characteristic peaks of C–C, C–O–C, and C–F bonds, respectively [40].

The O 1s XPS spectra of NiO/$Ti_3C_2T_x$ could be deconvoluted into three peaks at 529.1, 530.8 and 532.5 eV, which are ascribed to Ni–O, Ti–O–Ti, and Ti–OH, respectively. The deconvoluted F 1s spectrum of NiO/$Ti_3C_2T_x$ hybrid presented in Fig. S2. In general, a small amount of –F functional groups may come during the etching process of MXene. The peaks at 684.7 and 686.9 eV can be assigned to C–Ti-F_x and AlF_x functional groups, respectively [41]. The presence of –F and –OH functional groups could increase the interlayer spacing of $Ti_3C_2T_x$ sheets (as shown in Fig. 2(f)) and enhance the electroactive sites of the NiO/$Ti_3C_2T_x$ for better ion diffusion and electron transport during electrochemical redox reactions. The peaks of a Ni 2p spectrum (Fig. 4 (b and c) can be found around 853.7 and 872.3 eV, which linked to Ni $2p_{3/2}$ and Ni $2p_{1/2}$ core levels, respectively. The peak splitting between these core levels is 18.1 eV and exactly matches with the states of NiO [42]. Meanwhile, the other two minor peaks located at 860.9 and 878.5 eV could be assigned to the satellite peaks of NiO.

3.2. Supercapacitor performance

The electrochemical properties of as-prepared NiO and NiO/$Ti_3C_2T_x$ composite were investigated using cyclic voltammetry (CV), galvanostatic charge-discharge (GCD) and electrochemical impedance spectroscopy (EIS) analysis. A pair of redox peaks in the CV profiles (Fig. 5 a-d) indicate the battery-type characteristics of the electrodes resulting from the faradaic redox reactions. The oxidation peak is observed at 0.39 V, possibly due to the conversion of NiO to NiOOH (equation (1)), and the reduction peak is observed at 0.20 V due to the reverse reaction. The potential charge storage of NiO electrodes can be explained from the following redox mechanism [43].

$$NiO + OH^- \leftrightarrow NiOOH + e^- \quad (1)$$

As the evidence of Fig. 5(a–d), the cathodic and anodic peaks shift to lower and higher potential value as the scan rate increases, respectively, which is mainly due to the increase in Ohmic resistance of the electrode during the redox reactions. However, there are no apparent changes observed in the symmetry of redox peaks as the scan rate increase, demonstrating the quasi-reversibility of the redox process that derived from the porous structure of the NiO microspheres [44]. The CV curves of NiO/$Ti_3C_2T_x$ electrode exhibit the largest integral area and higher current density which reflect its higher specific capacity thanks to intercalation pseudocapacitance contribution of $Ti_3C_2T_x$ (Fig. 5 (d)). The ion-intercalation/de-intercalation phenomenon of $Ti_3C_2T_x$ associated with the surface redox reaction can be explained by the following expression [11],

$$Ti_3C_2(OH) + K^+ + e^- \leftrightarrow KTi_3C_2(OH) \quad (2)$$

In order to investigate the charge storage mechanism of the electrodes, the plot of log (i) versus log (ν) derived by the power law [45].

$$i = a\nu^b \quad (3)$$

where "i" is the measured current (A), "ν" is the scan rate (mV s^{-1}), "a" and "b" are the adjustable parameters. The slope of log (i) and log (v) plot referred to the value of "b". Fig. 5 (e) represents the plot of log (i) versus log (ν) of the electrodes. After fitting, it is found that the "b" values are about 0.57 and 0.41 at 0.3 V for NiO/$Ti_3C_2T_x$ and bare NiO, respectively. In general, "b = 0.5" indicates the battery-type behavior due to ion-intercalation/de-intercalation process,

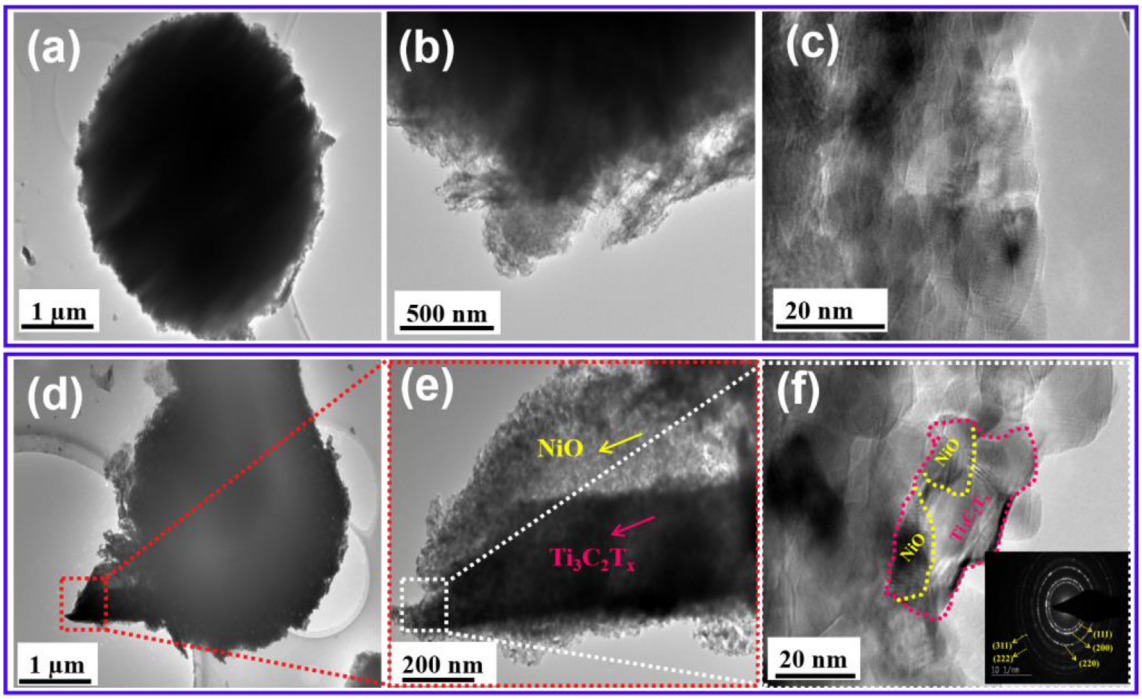

Fig. 3. TEM images of (a–c) NiO and (d–f) NiO/$Ti_3C_2T_x$ hybrid nanostructure.

whereas "b = 1" suggests a pseudocapacitance nature [12]. Thus, the charge storage mechanism of as prepared NiO/$Ti_3C_2T_x$ electrode is a diffusion-controlled intercalation/de-intercalation process.

Additionally, the charge storage behavior and the long-term cyclic stability of the electrodes were investigated by galvanostatic charge-discharge analysis. The discharge curves of the electrodes at different current densities are shown in Fig. 6(a–c). Obviously, the non-linear behavior and the voltage plateau of the discharge curves have been observed, reveals the battery-type faradaic behavior of the electrodes which is consistent with the CV measurements. The discharge time of NiO/$Ti_3C_2T_x$ is longer than bare NiO and $Ti_3C_2T_x$ in all current densities, suggesting that the higher specific capacity characteristic of NiO/$Ti_3C_2T_x$ electrode. The specific capacity, C (C g^{-1}) of the electrodes was calculated from the discharge curve by the following expression [46].

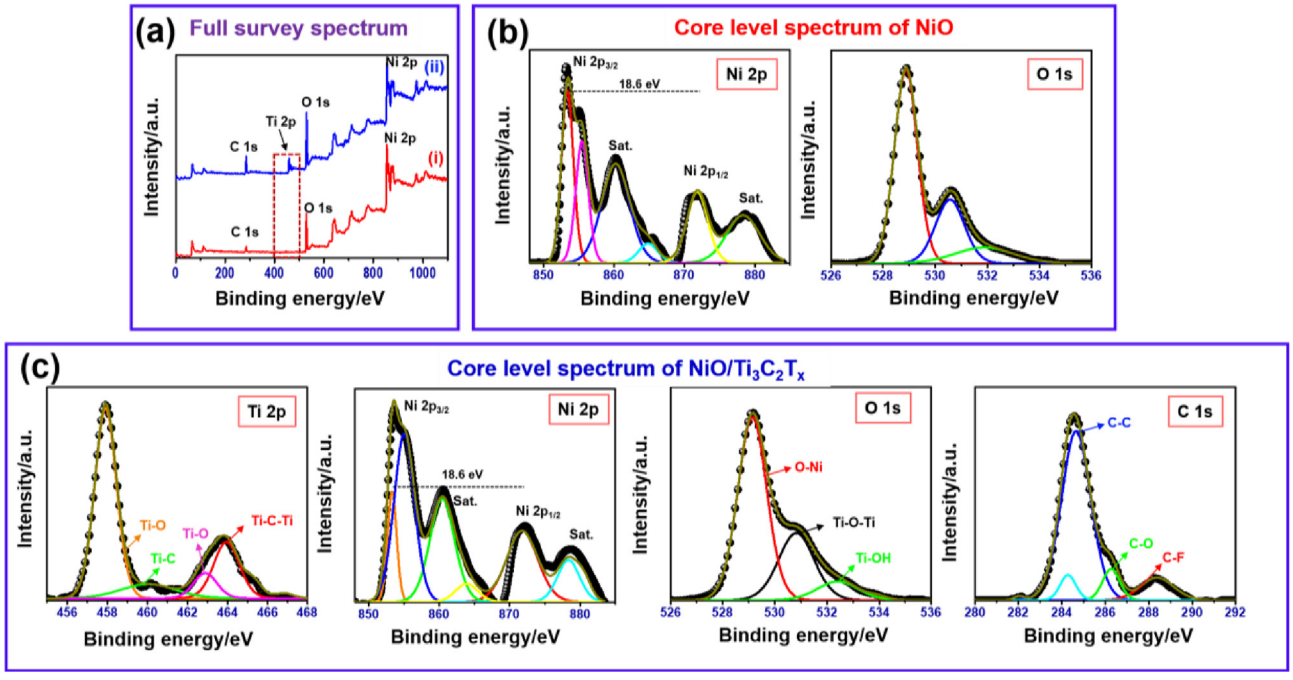

Fig. 4. (a) Full survey XPS spectrum of (i) NiO and (ii) NiO/$Ti_3C_2T_x$ (b) Core level XPS spectrum of NiO (c) Core level XPS spectrum of NiO/$Ti_3C_2T_x$ hybrid.

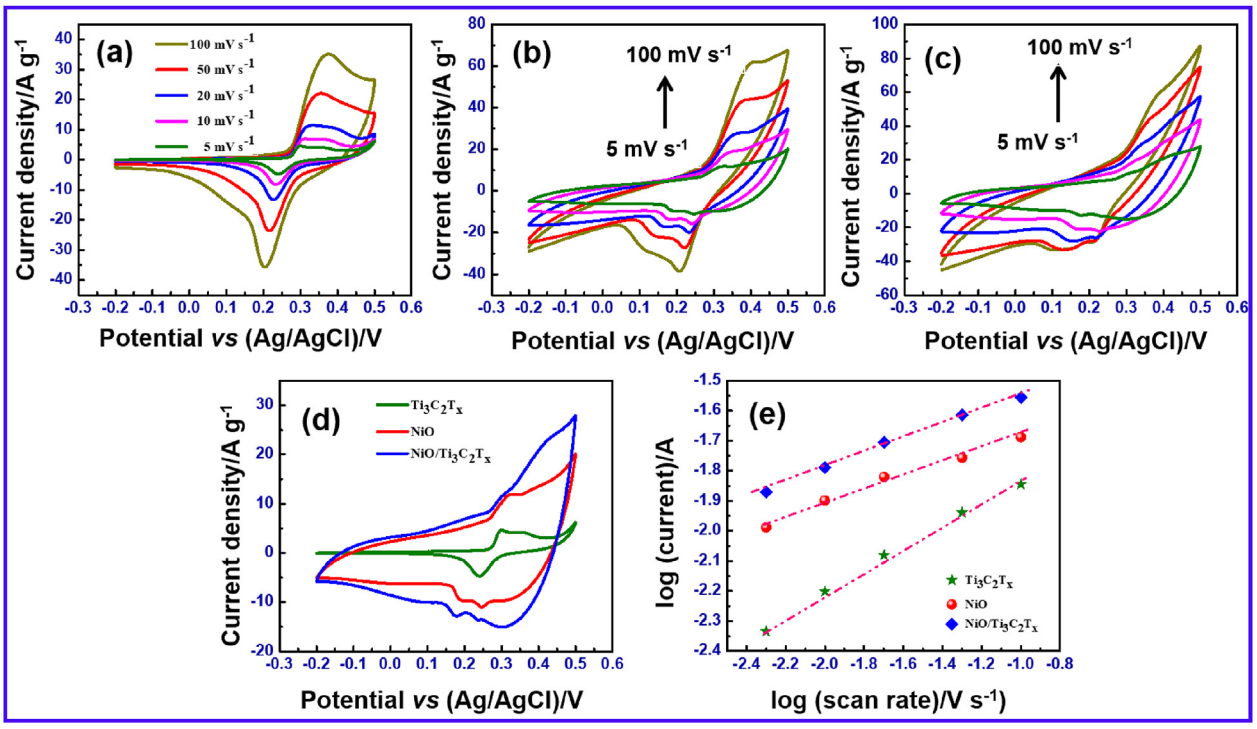

Fig. 5. Cyclic voltammetry response of (a) $Ti_3C_2T_x$ (b) NiO (c) NiO/$Ti_3C_2T_x$ (d) Comparison of CV response at 5 mV s^{-1} scan rate, and (e) Plot of log (i) versus log (ν).

$$C = \frac{I \times \Delta t}{m} \quad (4)$$

where I is the constant current (A), Δt is the discharge time, and m is the mass of the active material (g).

As the evidence of Fig. 6 (d and e), NiO/$Ti_3C_2T_x$ electrode delivers a maximum specific capacity of 630.9C g^{-1} (175.2 mA h g^{-1}) at a current density of 1 A g^{-1}, which is significantly higher than that of pure NiO (376.8C g^{-1}, 104.6 mA h g^{-1}) and $Ti_3C_2T_x$ (37.9C g^{-1}, 10.5 mA h g^{-1}), respectively. It can be seen that the specific capacity decreases with increasing current density. The decrease in specific

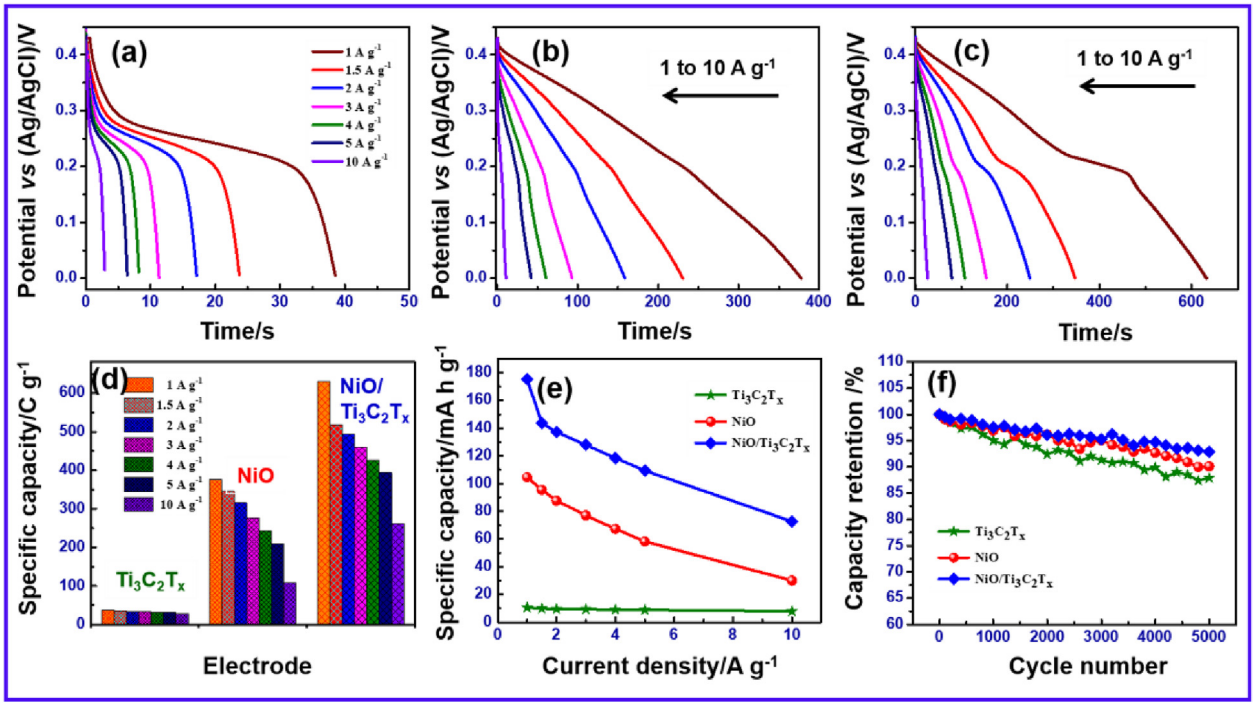

Fig. 6. Galvanostatic discharge curves at different current densities (a) $Ti_3C_2T_x$ (b) NiO (c) NiO/$Ti_3C_2T_x$, and (d, e) Specific capacity of the electrodes as function of the current density (f) Capacity retention behavior of the different electrodes at a current density of 2 A g^{-1}.

Table 1
Comparison of electrochemical performance of different NiO based electrodes.

Electrode	*Electrolyte*	*Performance*	*Cyclic performance*	*Ref*
NiO nanourchins	3 M KOH	540.5 F g^{-1} at 1 A g^{-1}	79.9% after 1000 cycles at 10 A g^{-1}	[48]
S–NiO	1 M KOH	313 F g^{-1} at 5 mV s^{-1}	99% after 1000 cycles at 40 mV s^{-1}	[49]
NiO	1 M KOH	449 F g^{-1} 5 m V s^{-1}	74% after 500 cycles at 6 A g^{-1}	[50]
NiO/graphene aerogel	6 M KOH	587.3 F g^{-1} at 1 A g^{-1}	98.5% after 1000 cycles at 1 A g^{-1}	[51]
NiO/N-doped carbon hollow sphere	2 M KOH	585 F g^{-1} at 1 A g^{-1}	100% after 6000 cycles at 5 A g^{-1}	[52]
Cs@NiO	3 M KOH	825 F g^{-1} at 1 A g^{-1}	85% after 3500 cycles at 10 A g^{-1}	[53]
HNCS–NiO	1 M KOH	550.4 F g^{-1} at 0.5 A g^{-1}	83.4% after 2000 cycles at 10 A g^{-1}	[54]
NiO/graphene	2 M KOH	1062 F g^{-1} at 1 A g^{-1}	90.6% after 5000 cycles at 1 A g^{-1}	[55]
NiO/rGO	1 M KOH	590 F g^{-1} at 1 A g^{-1}	100% after 1000 cycles at 1 A g^{-1}	[56]
NiO/Graphene	6 M KOH	555 F g^{-1} at 1 A g^{-1}	90.8% after 2000 cycles at 1 A g^{-1}	[57]
NiO/Co_3O_4 core/shell composite	6 M KOH	255C g^{-1} at 5 mA cm^{-2}	92% after 1000 cycles at 5 mA cm^{-2}	[58]
NiO	**3 M KOH**	**376.8 C g^{-1} at 1 A g^{-1}**	**90.1% after 5000 cycles at 1 A g^{-1}**	**This work**
NiO/$Ti_3C_2T_x$	**3 M KOH**	**630.9 C g^{-1} at 1 A g^{-1}**	**92.9% after 5000 cycles at 1 A g^{-1}**	**This work**

capacity was attributed to the limited utilization of the inner and outer surface of the active material by OH- ions [47]. On the other hand, the electrolyte ions have sufficient time to access the inner surface, which leads to the high specific capacity. In addition, areal capacity (C cm^{-2}) is an essential factor for supercapacitor application, the electrode areal capacity was calculated according to the following equation [46].

$$C = \frac{I \times \Delta t}{S} \quad (5)$$

where S is the area of the electrode (cm^2). As illustrated in Fig. S3, the NiO/$Ti_3C_2T_x$ electrode exhibits remarkably higher areal capacity (1.261C cm^{-2}), which further confirms the excellent charge storage behavior. A comparison is made between other reported NiO based materials and the current work, as shown in Table 1.

The electrochemical cyclic stability of the electrodes was investigated by GCD technique at a current density of 2 A g^{-1} over 5000 cycles (as shown in Fig. 6 (f)). The capacity retention of nearly 92.9% is obtained over 5000 cycles for NiO/$Ti_3C_2T_x$ hybrids, which shows excellent stability performance than bare NiO and $Ti_3C_2T_x$ electrodes. These results prove that the introduction of the 2D structured $Ti_3C_2T_x$ into NiO can significantly enhance the electrochemical stability as a result of high accessibility of the electrode surface to electrolyte ions [59]. However, a small decrease (~7%) in specific capacity of NiO/$Ti_3C_2T_x$ hybrid which might be due to the stacking effect of $Ti_3C_2T_x$ layers over prolonged charge/discharge cycles resulting in the slow diffusion rate of electrolyte ions during insertion/de-insertion process.

Furthermore, the electrochemical characteristic of the electrode/electrolyte interface of the as-prepared electrodes was investigated by electrochemical impedance spectroscopy (EIS) in the frequency range from 1 Hz to 10^5 Hz. Fig. 7 (a) represents the Nyquist plots of NiO, $Ti_3C_2T_x$ and NiO/$Ti_3C_2T_x$ hybrids. The point of the intersection curves at the real axis in the high-frequency region is known as the internal resistance (R_s), which includes the intrinsic resistance of the active material, contact resistance at the interface between the active material and the current collector, and the electrolyte resistance [60]. As from Fig. 7 (a) and Table 2, the internal resistance of NiO/$Ti_3C_2T_x$ electrode is found to be 0.85 Ω

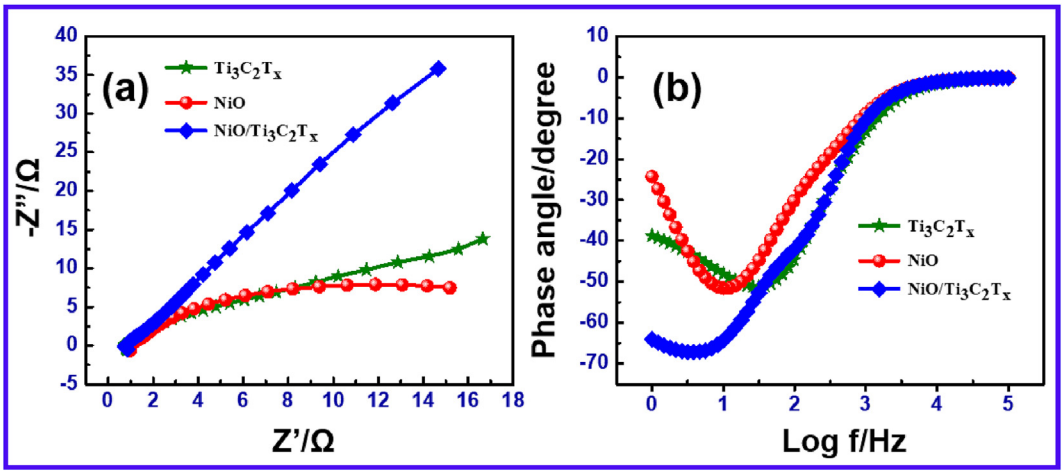

Fig. 7. (a) Nyquist plot of the electrodes from the frequency range 1 Hz–10^5 Hz (b) Bode phase angle plot of $Ti_3C_2T_x$, NiO and NiO/$Ti_3C_2T_x$ electrode.

Table 2
Various observed electrochemical performance of $Ti_3C_2T_x$, NiO and NiO/$Ti_3C_2T_x$ electrodes.

Electrode	*Specific capacity/C g^{-1}*	*Specific capacity/mA h g^{-1}*	*Areal capacity/C cm^{-2}*	*Solution resistance R_s/Ω*
Ti_3C_2Tx	37.9	10.5	0.075	0.91
NiO	376.8	104.6	0.754	0.98
NiO/$Ti_3C_2T_x$	630.9	175.2	1.261	0.85

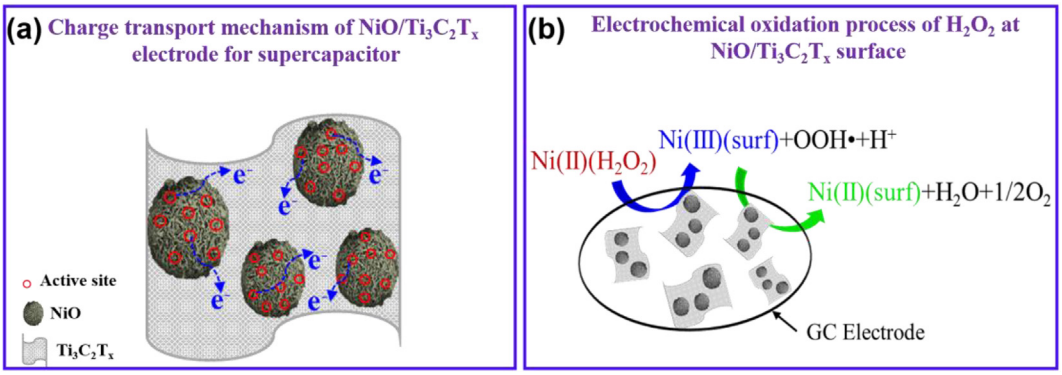

Fig. 8. (a) Charge transport mechanism of NiO/$Ti_3C_2T_x$ electrode for supercapacitor (b) Electrochemical oxidation process of H_2O_2 at NiO/$Ti_3C_2T_x$ modified glassy-carbon electrode surface.

which is lower than that of pure NiO (0.98Ω) and $Ti_3C_2T_x$ (0.91Ω), suggesting the better ion diffusion at the NiO/$Ti_3C_2T_x$ electrode/electrolyte interface. The straight line at a lower frequency is related to the characteristic of frequency dependent on diffusion kinetics of electrolyte ions to the electroactive area, which is called as "Warburg resistance" [61]. It can be seen from the plot that the Warburg line of the NiO/$Ti_3C_2T_x$ is closer to the imaginary axis, which suggests the ideal capacitive behavior due to their synergistic effect. Fig. 7 (b) represents the Bode phase angle plot of all the electrodes. It can be seen that the bode phase angle of NiO/$Ti_3C_2T_x$ electrode is about 68.42° at the low-frequency region, which reveals the excellent capacity nature than bare NiO and $Ti_3C_2T_x$ electrodes.

The high electrochemical activity of NiO/$Ti_3C_2T_x$ can be explained as follows: (i) The majority of NiO microspheres are attached on the surface of $Ti_3C_2T_x$, which stabilizes NiO and provides more active sites for the electrolyte ions as shown in Fig. 8 (a), therefore facilitates the electron transportation compared with

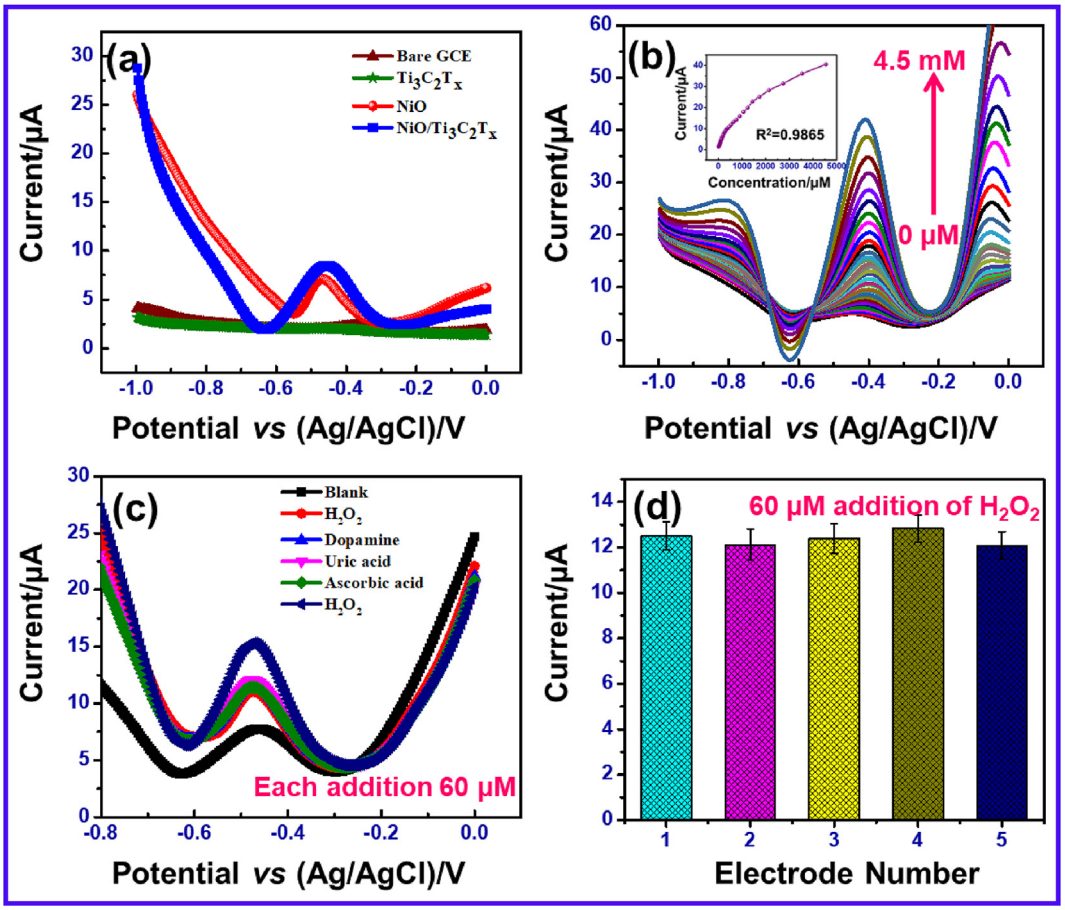

Fig. 9. (a) Comparison of DPV response of the electrodes modified differently in the presence of 60 μM concentration of H_2O_2 (b) DPV response of NiO/$Ti_3C_2T_x$ modified electrode for different concentration of H_2O_2 (Inset picture: Linear response of the current versus H_2O_2 concentrations) (c) Interference analysis of NiO/$Ti_3C_2T_x$ modified electrode in the presence of other interfering compounds and (d) The reproducibility of NiO/$Ti_3C_2T_x$ modified electrode for five different electrodes.

Table 3
Analytical performance characteristics for other NiO based electrochemical sensors reported for H_2O_2 detection.

Electrode	*Detection limit (μM)*	*Linear range*	*Ref*
NiO/graphene	0.7664	0.25 mM–4.75 mM	[63]
NiO nanosheet/Graphite sheet	0.4	Up to 4 mM	[67]
NiO film/Graphite sheet	4.8	Up to 2.5 mM	[67]
NiO/ITO	1.28 mM	0.01–1 mM	[68]
$Ti_3C_2T_x$	883	–	[69]
$Ti_3C_2T_x$/PtNP–S 2.75%	0.448	–	[69]
NiO	**5.40**	**0.01–0.57 mM**	**This work**
NiO/$Ti_3C_2T_x$	**0.348**	**0.01–4.54 mM**	**This work**

pure NiO; (ii) The cations (K^+) favors intercalation between the interlayer voids of $Ti_3C_2T_x$ (indicated in Fig. 2 f) and hence enhance the intercalation-pseudocapacity of $Ti_3C_2T_x$.

3.3. Electrochemical detection of H_2O_2

Differential pulse voltammetry (DPV) analysis was utilized for H_2O_2 detection, which serves with remarkable sensitivity and better electrochemical technique compared to other voltammetry analysis due to several merits like high sensitivity, negative redox peak potential and rapid response [62]. Fig. 9(a), demonstrates the DPV response of three electrodes modified with different materials along with bare GC electrode in the presence of 60 μM H_2O_2 containing 0.5 M of NaOH. It has been noted that the electrochemical current of NiO modified electrode shows higher response than bare glassy-carbon electrode (GCE) in the oxidation process by H_2O_2 which concludes that the NiO exhibits excellent electrocatalytic activity [63]. Interestingly, after incorporation of $Ti_3C_2T_x$ into NiO, a notable enhancement in the current response with broader oxidation potential was observed. The improved peak current and greater electrocatalytic activity of H_2O_2 may be associated with the combined unique properties of NiO and $Ti_3C_2T_x$.

From the BET analysis above, $Ti_3C_2T_x$ affords a higher surface area, which can promote the electrocatalytic activity of NiO based sensor [64]. It is noteworthy that $Ti_3C_2T_x$ also prevents the NiO/$Ti_3C_2T_x$ modified electrode from any fouling and leaching effects, thus enhances the electron transfer at the electrode surface [65]. Fig. 9 (b) shows the DPV response of NiO/$Ti_3C_2T_x$ modified electrode with the addition of various concentration of H_2O_2. The obtained outcomes indicate that the H_2O_2 oxidation peak current gradually increased with increasing concentration of H_2O_2 from 0 μM to 4.5 mM. In addition, the modified electrode possesses an

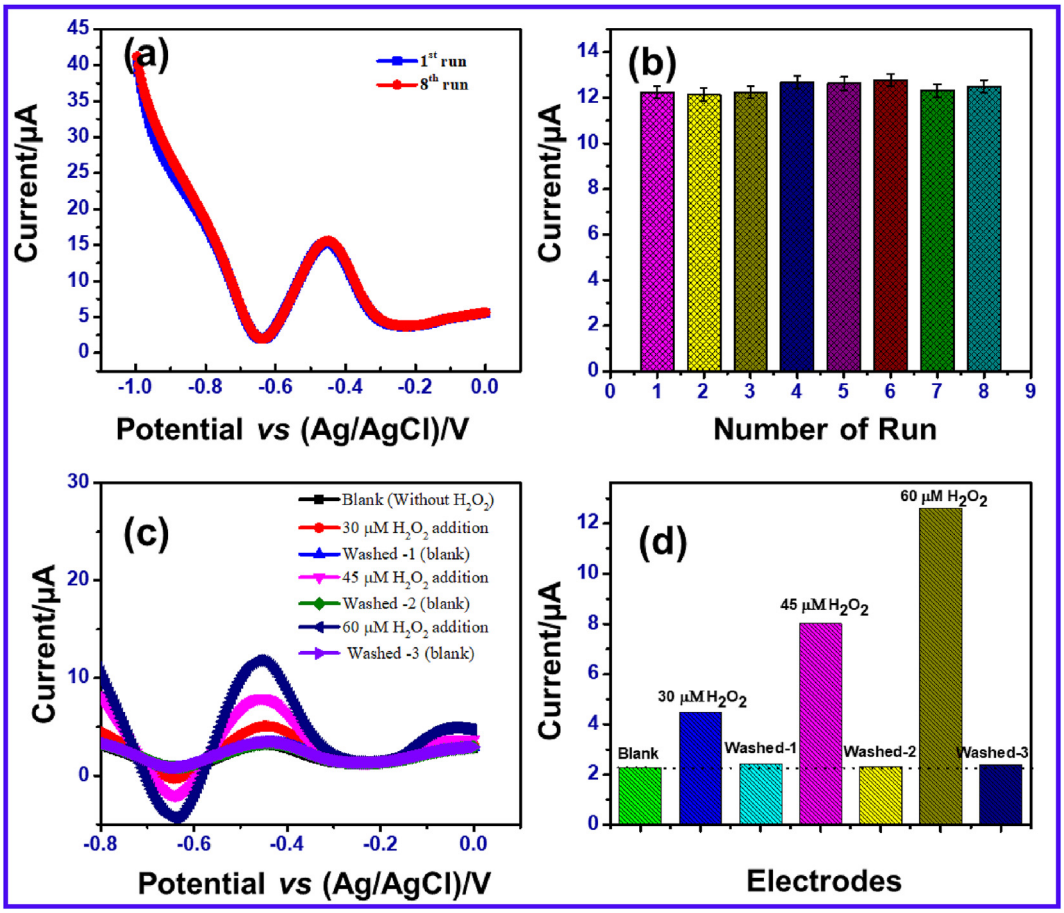

Fig. 10. (a & b) The stability of the NiO/$Ti_3C_2T_x$ modified electrode in the presence of 60 μM H_2O_2 in 0.5 M NaOH solution for eight consecutive measurements (c & d) Stability of NiO/$Ti_3C_2T_x$ modified electrode before and after washing towards detection of H_2O_2 at various concentrations.

excellent linear response for H_2O_2 concentration ranging from 10 μM to 4.5 mM with a correlation coefficient of 0.9865 (Inset pictures of Fig. 9 (b)). The H_2O_2 oxidation current of NiO can be obtained from the electron transfer of Ni(II) to Ni(III) redox states [66]. Fig. 8 (b) shows the whole electrochemical oxidation process of H_2O_2 at NiO/$Ti_3C_2T_x$ modified electrode surface. Whereas, NiO modified electrode displays a short linear response ranging only from 10 μM to 0.57 mM (Fig. S4), hinting that the presence of $Ti_3C_2T_x$ could improve the electrocatalytic activity. By reviewing these results, it clearly shows that the $Ti_3C_2T_x$ is not only enhancing the broader range concentration of H_2O_2 detection, it is also responsible at low concentration of H_2O_2. i,e, the detection limit of NiO/$Ti_3C_2T_x$ modified electrode is down to 0.34 μM which is considerably lower than that of NiO sensor detection limit (5.40 μM). Table 3 shows a comparison of the analytical performance of the NiO based H_2O_2 sensor.

The avoidance of interfering reactants is an essential and quite challenging fact in the electrochemical sensor field. In this view, the selectivity evaluation of NiO/$Ti_3C_2T_x$ modified electrode was studied using DPV technique in the presence of common interfering compounds such as dopamine, uric acid and ascorbic acid (Fig. 9 (c)). The oxidation peak current of the injected interfering compounds is nearly negligible compared with H_2O_2 peak current, which illustrates that the proposed electrode has excellent selectivity towards H_2O_2 detection. The reproducibility of the NiO/$Ti_3C_2T_x$ sensor was investigated by detecting 60 μM H_2O_2 with five different GCE electrodes and the current response of the five GCE electrodes have exhibited almost identical response towards H_2O_2 detection under the same test conditions (Fig. 9 (d)), which implies the reproducible property of NiO/$Ti_3C_2T_x$. The proposed NiO/$Ti_3C_2T_x$ sensor not only manifested excellent reproducibility but also demonstrated good repeatability towards detection of H_2O_2. As evidence from Fig. 10 (a and b), NiO/$Ti_3C_2T_x$ modified electrode exhibited an acceptable and very close current response for eight consecutive measurements. These results prove that the NiO/$Ti_3C_2T_x$ modified electrode has an excellent electrocatalytic activity for H_2O_2 detection and it could be employed for the low detection limit of H_2O_2.

Fig. 10 c & d shows the stability and response of the NiO/$Ti_3C_2T_x$ modified electrode for H_2O_2 detection at various concentrations. The experiment carried out using DPV technique in the presence of H_2O_2 before and after washing the electrode. The modified electrode shows an excellent response to the detection. This led to a remarkable acceleration in the rate of electrochemical oxidation of H_2O_2. There was no significant change in the response even after washing the electrode. These results indicate improved stability NiO/$Ti_3C_2T_x$ modified electrode towards the detection and determination of H_2O_2.

4. Conclusion

In summary, the porous architecture of NiO on $Ti_3C_2T_x$ has been prepared from Ni-MOF/$Ti_3C_2T_x$ hybrid by simple calcination process, and the as-prepared hybrid was analyzed with different characterization techniques. The prepared electrode showed excellent electrochemical response towards supercapacitor and non-enzymatic H_2O_2 detection applications. A maximum specific capacity of 630.9C g^{-1} has been achieved for NiO/$Ti_3C_2T_x$ electrode which suggests a promising battery-type electrode for supercapacitor. The presence of $Ti_3C_2T_x$ could provide more active sites of NiO for redox reaction, which improves the capacity behavior. Furthermore, $Ti_3C_2T_x$ prevented the NiO/$Ti_3C_2T_x$ modified electrode from fouling and leaching effect, which could help to achieve low detection limit (0.34 μM) with a wide detection range of H_2O_2 concentration for the electrochemical non-enzymatic H_2O_2 sensor. This work demonstrates that the prepared NiO/$Ti_3C_2T_x$ hybrid could be applied for both high-performance supercapacitor and highly sensitive H_2O_2 sensor applications.

Acknowledgment

This work was supported by Special Funds for the Development of Strategic Emerging Industries in Shenzhen (JCYJ20170412154240645, 2017), and Shenzhen Science and Technology Innovation Committee (Projects No. JCYJ20170412154426330). Fei Wang is supported by Guangdong Natural Science Funds for Distinguished Young Scholar (Projects No. 2016A030306042), and the Guangdong Special Support Program under (Projects No. 2015TQ01X555).

Appendix A. Supplementary data

Supplementary data to this article can be found online at https://doi.org/10.1016/j.electacta.2019.134771.

References

[1] Y. Song, X. Li, L. Sun, L. Wang, Metal/metal oxide nanostructures derived from metal−organic frameworks, RSC Adv. 5 (2015) 7267−7279.
[2] W. Xia, A. Mahmood, R. Zou, Q. Xu, Metal−organic frameworks and their derived nanostructures for electrochemical energy storage and conversion, Energy Environ. Sci. 8 (2015) 1837−1866.
[3] L. Liu, Y. Zhou, S. Liu, M. Xu, The applications of Metal-Organic frameworks in electrochemical sensors, Chem. Electro. Chem. 2 (2018) 6−19.
[4] Q. Wang, F. Gao, B. Xu, F. Cai, F. Zhan, F. Gao, Q. Wang, ZIF-67 derived amorphous $CoNi_2S_4$ nanocages with nanosheet arrays on the shell for a high-performance asymmetric supercapacitor, Chem. Eng. J. 327 (2017) 387−396.
[5] Y. Yang, F. Yang, H. Hu, S. Lee, Y. Wang, H. Zhao, D. Zeng, B. Zhou, S. Hao, Dilute NiO/carbon nanofiber composites derived from metal organic framework fibers as electrode materials for supercapacitors, Chem. Eng. J. 307 (2017) 583−592.
[6] T. Brousse, D. Belanger, J.W. Long, To be or Not to be Pseudocapacitive, J. Electrochem. Soc. 5 (2015) A5185−A5189.
[7] P. Wen, P. Gong, J. Sun, J. Wang, S. Yang, Design and synthesis of Ni-MOF/CNT composites and rGO/carbon nitride composites for an asymmetric supercapacitor with high energy and power density, J. Mater. Chem. 3 (2015) 13874−13883.
[8] R. Ramachandran, W. Xuan, C. Zhao, X. Leng, D. Sun, D. Luo, F. Wang, Enhanced electrochemical properties of cerium metal−organic framework based composite electrodes for high-performance supercapacitor application, RSC Adv. 8 (2018) 3462−3469.
[9] K. Rajavel, T. Ke, K. Yang, D. Lin, Condition optimization for exfoliation of two dimensional titanium carbide ($Ti_3C_2T_x$), Nanotechnology 29 (2018) 095605−095609.
[10] J. Li, X. Yuan, C. Lin, Y. Yang, L. Xu, X. Du, J. Xie, J. Lin, J. Sun, Achieving high pseudocapacitance of 2D titanium carbide (MXene) by cation intercalation and surface modification, Adv. Energy Mater. 7 (2017) 1602725.
[11] R. Ramachandran, K. Rajavel, W. Xuan, D. Lin, F. Wang, Influence of $Ti_3C_2T_x$ (MXene) intercalation pseudocapacitance on electrochemical performance of Co-MOF binder-free electrode, Ceram. Int. 44 (2018) 14425−14431.
[12] P. Pazhamalai, K. Krishnamoorthy, V.K. Mariappan, S.J. Kim, Blue TiO_2 nanosheets as a high-performance electrode material for supercapacitors, J. Colloid Interface Sci. 536 (2019) 62−70.
[13] J. Gao, X. Cai, J. Wang, M. Hou, L. Lai, L. Zhang, Recent progress in hierarchically structured O_2-cathodes for Li-O_2 batteries, Chem. Eng. J. 352 (2018) 972−995.
[14] W. Deng, Y. Li, Electrochemical sensor for determining the manganese content in molten iron, Electrochim. Acta 265 (2018) 265−274.
[15] C. Zhu, G. Yang, H. Li, D. Du, Y. Lin, Electrochemical sensors and biosensors based on nanomaterials and nanostructures, Anal. Chem. 87 (2015) 230−249.
[16] K. Krishnamoorthy, P. Pazhamalai, S.J. Kim, Ruthenium sulfide nanoparticles as a new pseudocapacitive material for supercapacitor, Electrochim. Acta 227 (2017) 85−94.
[17] R. Ramachandran, C. Zhao, D. Luo, K. Wang, F. Wang, Morphology-dependent electrochemical properties of cobalt-based metal organic frameworks for supercapacitor electrode materials, Electrochim. Acta 267 (2018) 170−180.
[18] Z. Wu, L.P. Sun, Z. Zhou, Q. Li, L.H. Huo, H. Zhao, Efficient nonenzymatic H2O2 biosensor based on ZIF-67 MOF derived Co nanoparticles embedded N-doped mesoporous carbon composites, Sens. Actuators, B 276 (2018) 142−149.
[19] L. Ning, X. Guan, J. Ma, M. Wang, X. Fan, G. Zhang, F. Zhang, W. Peng, Y. Li, A highly sensitive nonenzymatic H_2O_2 sensor based on platinum, $ZnFe_2O_4$ functionalized reduced graphene oxide, J. Alloy. Comp. 738 (2018) 317−322.
[20] E.M. Elnemma, Spectrophotometric determination of hydrogen peroxide by a hydroquinone-aniline system catalyzed by molybdate, Bull. Korean Chem.

Soc. 25 (2004) 127–129.
[21] H.S. Marinho, C. Real, L. Cyrne, H. Soares, F. Antunes, Hydrogen peroxide sensing, signaling and regulation of transcription factors, Redox Biol. 2 (2014) 535–562.
[22] S. Hanaoka, J.-M. Lin, M. Yamada, Chemiluminescent flow sensor for H_2O_2 based on the decomposition of H_2O_2 catalyzed by cobalt(II)-ethanolamine complex immobilized on resin, Anal. Chim. Acta 426 (2001) 57–64.
[23] S. Yang, G. Li, G. Wang, L. Liu, D. Wang, L. Qu, Synthesis of highly dispersed CeO_2 nanoparticles on N-doped reduced oxide graphene and their electrocatalytic activity toward H_2O_2, J. Alloy. Comp. 688 (2016) 910–916.
[24] K. Bindu, K. Sridharan, K.M. Ajith, H.N. lim, H.S. Nagaraja, Microwave assisted growth of stannous ferrite microcubes as electrodes for potentiometric nonenzymatic H_2O_2 sensor and supercapacitor applications, Electrochim. Acta 217 (2016) 139–149.
[25] H. Dai, W. Lu, X. Zuo, Q. Zhu, C. Pan, X. Niu, J. Liu, H. Chen, X. Chen, A novel biosensor based on boronic acid functionalized metal-organic frameworks for the determination of hydrogen peroxide released from living cells, Biosens. Bioelectron 95 (2017) 131–137.
[26] J. Cai, S. Ding, G. Chen, Y. Sun, Q. Xie, In situ electrodeposition of mesoporous aligned α-Fe_2O_3 nanoflakes for highly sensitive nonenzymatic H_2O_2 sensor, Appl. Surf. Sci. 456 (2018) 302–306.
[27] S.J. Li, J.C. Zhang, J. Li, H.Y. Yang, J.J. Meng, B. Zhang, A 3D sandwich structured hybrid of gold nanoparticles decorated MnO_2/graphene-carbon nanotubes as high performance H_2O_2 sensors, Sens. Actuators, B 260 (2018) 1–11.
[28] E.E. Miller, Y. Hua, F.H. Tezel, Materials for energy storage: review of electrode materials and methods of increasing capacitance for supercapacitors, J. Energy Storage 20 (2018) 30–40.
[29] C. Peng, S. Zhou, X. Zheng, T. Zeng, W. Zhang, H. Li, X. Liu, P. Zhao, One pot synthesis of nitrogen-doped hollow carbon spheres with improved electrocatalytic properties for sensitive H_2O_2 sensing in human serum, Sens. Actuators, B 270 (2018) 530–537.
[30] D. Han, P. Xu, X. Jing, J. Wag, D. Song, J. Liu, M. Zhang, Facile approach to prepare hollow core-shell NiO microspheres for supercapacitor electrodes, J. Solid State Chem. 203 (2013) 60–67.
[31] Y. Wang, H. Dou, J. Wang, B. Ding, Y. Xu, Z. Chang, X. Hao, Three-dimensional porous MXene/layered double hydroxide composite for high performance supercapacitors, J. Power Sources 327 (2016) 221–228.
[32] R. Ramachandran, M. Saranya, P. Kollu, B.P.C. Raghupathy, S.K. Jeong, A.N. Grace, Solvothermal synthesis of Zinc sulfide decorated Graphene (ZnS/G) nanocomposites for novel Supercapacitor electrodes, Electrochim. Acta 178 (2015) 647–657.
[33] G. Zhou, J. Zhu, Y.J. Chen, L. Mei, X.C. Duan, G.H. Zhang, L.B. Chen, T.H. Wang, B.G. Lu, Simple method for the preparation of highly porous $ZnCo_2O_4$ nanotubes with enhanced electrochemical property for supercapacitor, Electrochim. Acta 123 (2014) 450–455.
[34] C. An, Y. Wang, Y. Huang, Y. Xu, L. Jiao, H. Yuan, Porous $NiCo_2O_4$ nanostructures for high performance supercapacitors via a micro emulsion technique, Nano Energy 10 (2014) 125–134.
[35] Z. Lin, Y. Yang, J. Jin, L. Wei, W. Chen, Y. Lin, Z. Huang, Graphene- wrapped $Li_4Ti_5O_{12}$ hollow spheres consisting of nanosheets as novel anode material for lithium-ion batteries, Electrochim. Acta 254 (2017) 287–298.
[36] Q. Xu, L. Diang, Y. Wen, W. Yang, H. Zhou, X. Chen, J. Street, A. Zhou, W.-J. Ong, N. Li, High photoluminescence quantum yield of 18.7% by using nitrogen-doped Ti_3C_2 MXene quatum dots, J. Mater. Chem. C 6 (2018) 6360–6369.
[37] Y. Wang, Y. Li, Z. Qiu, X. Wu, P. Zhou, T. Zhou, J. Zhao, Z. Miao, J. Zhou, S. Zhuo, Fe_3O_4@Ti_3C_2 MXene hybrids with ultrahigh volumetric capacity as an anode material for lithium-ion batteries, J. Mater. Chem. 6 (2018) 11189–11197.
[38] W. Bao, X. Xie, J. Xu, X. Guo, J. Song, W. Wu, D. Su, G. Wang, Confined sulphur in 3D MXene/Reduced graphene oxide hybrid nanosheets for lithium-sulfur battery, Chem. Eur J. 23 (2017) 12613–12619.
[39] Q. Xue, Z. Pei, Y. Huang, M. Zhu, Z. Tang, H. Li, Y. Huang, N. Li, H. Zhang, C. Zhi, Mn_3O_4 nanoparticles on layer-structured Ti_3C_2 MXene towards the oxygen reduction reaction and zinc–air batteries, J. Mater. Chem. 5 (2017) 20818–20823.
[40] C. Shen, L. Wang, A. Zhou, H. Zhang, Z. Chen, Q. Hu, G. Qin, MoS_2-Decorated Ti_3C_2 MXene nanosheets as anode material in lithium-ion batteries, J. Electrochem. Soc. 164 (2017) A2654–A2689.
[41] S.A. Shah, T. Habib, P. Gao, W. Sun, M.J. Green, M. Radovic, Template-free 3D titanium carbide ($Ti_3C_2T_x$) MXene particles crmpled by capillary forces, Chem. Commun. 53 (2017) 400–403.
[42] V.S. Kumbhar, M.H. Cho, J. Lee, W.K. Kim, M. Lee, Y.R. Lee, J.J. Shim, Electrosynthesis of a corn flake-like NiO nanostructure on nickel foam for polymer gel electrolyte-based high performance asymmetric supercapacitors, New J. Chem. 41 (2017) 10584–10591.
[43] X. Hui, L. Qian, G. Harris, T. Wang, J. Che, Fast fabrication of NiO@graphene composites for supercapacitor electrodes: combination of reduction and deposition, Mater. Des. 109 (2016) 242–250.
[44] X.Y. Hou, X.L. Yan, X. Wang, Q.G. Zhai, Tuning the porosity of mesoporous NiO through calcining isostructural Ni-MOFs toward supercapacitor applications, J. Solid State Chem. 263 (2018) 72–78.
[45] J. Guo, Y. Zhao, A. liu, T. Ma, Electrostatic self-assembly of 2D delaminated MXene (Ti_3C_2) onto Ni foam with superior electrochemical performance for supercapacitor, Electrochim. Acta 305 (2019) 164–174.
[46] Y. Fan, Z. Ma, L. Wang, Y. Dong, T. Jiang, Z. Li, L. Liu, G. Shao, In-situ synthesis of NiO foamed sheets on Ni foam as efficient cathode of battery-type supercapacitor, Electrochim. Acta 269 (2018) 62–69.
[47] R. Ramachandran, C. Zhao, D. Luo, K. Wang, F. Wang, Synthesis of copper benzene-1, 3, 5-tricarboxylate metal organic frameworks with mixed phases as the electrode material for supercapacitor applications, Appl. Suf. Sci. 460 (2018) 33–39.
[48] Y. Zhang, J. Wang, H. Wei, J. Hao, J. Mu, P. Cao, J. Wang, S. Zhao, Hydrothermal synthesis of hierarchical mesoporous NiO nanourchins and their supercapacitor application, Mater. Lett. 162 (2016) 67–70.
[49] B.S. Singu, S.E. Hong, K.R. Yoon, Sulfur-doped nickel oxide spherical nanosheets for redox supercapacitors, J. Ind. Eng. Chem. 62 (2018) 321–328.
[50] N. Duraisamy, A. Numan, S.O. Fatin, K. Ramesh, S. Ramesh, Facile sonochemical synthesis of nanostructured NiO with different particle sizes and its electrochemical properties for supercapacitor application, J. Colloid Interface Sci. 471 (2016) 136–144.
[51] W. Chen, D. Gui, J. Liu, Nickel oxide/graphene aerogel nanocomposite as a supercapacitor electrode material with extremely wide working potential window, Electrochim. Acta 222 (2016) 1424–1429.
[52] T. Liu, C. Jiang, B. Cheng, W. You, J. Yu, Hierarchical flower-like C/NiO composite hollow microspheres and its excellent supercapacitor performance, J. Power Sources 359 (2017) 371–378.
[53] A.S. Justin, P. Vickraman, B.J. Reddy, Synthesis and characterization of high porous carbon sphere@nickel oxide core-shell nanocomposite for supercapacitor applications, J. Electroanal. Chem. 823 (2018) 342–349.
[54] Q. Li, C.L. Li, Y.L. Li, J.J. Zhou, C. Chen, R. Liu, L. Han, Fabrication of hollow N-doped carbon supported ultrathin NiO nanosheets for high-performance supercapacitor, Inorg. Chem. Commun. 86 (2017) 140–144.
[55] J. Lv, Z. Wang, H. Miura, Facile synthesis of mesoporous NiO nanoflakes on graphene foam and its electrochemical properties for supercapacitor application, Solid State Commun. 269 (2018) 45–49.
[56] H. Kahimbi, S.B. Hong, M. Yang, B.G. Choi, Simultaneous synthesis of NiO/reduced graphene oxide composites by ball milling using bulk Ni and graphite oxide for supercapacitor applications, J. Electroanal. Chem. 786 (2017) 14–19.
[57] B. Zhao, H. Zhuang, T. Fang, Z. Jiao, R. Liu, X. Ling, B. Lu, Y. Jinang, Self-assembly of NiO/graphene with three-dimension hierarchical structure as high performance electrode material for supercapacitors, J. Alloy. Comp. 597 (2014) 291–298.
[58] M. Fan, B. Ren, L. Yu, Q. Liu, J. Liu, J. Wang, X. Jing, L. Liu, Facile synthesis of Co_3O_4 nanowires grown on hollow NiO microspheres with superior electrochemical performance, Electrochim. Acta 166 (2015) 168–173.
[59] K.H. Oh, G.S. Gund, H.S. Park, Stabilizing $NiCo_2O_4$ hybrid architectures by reduced graphene oxide interlayers for improved cycling stability of hybrid supercapacitors, J. Mater. Chem. 6 (2018) 22106–22114.
[60] A.S. Justin, P. Vickraman, B.J. Reddy, Synthesis and characterization of high porous carbon sphere@nickel oxide core-shell nanocomposite for supercapacitor applications, J. Electroanal. Chem. 823 (2018) 342–349.
[61] P. Pazhamalai, K. Krishnamoorthy, S. Sahoo, S.J. Kim, Two-dimensional molybdenum diselenide nanosheets as a novel electrode material for symmetric supercapacitors using organic electrolyte, Electrochim. Acta 295 (2019) 591–598.
[62] T. Kokulnathan, T.S.K. Sharma, S.M. Chen, Y.H. Yu, Synthesis and characterization of zirconium dioxide anchored carbon nanofiber composite for enhanced electrochemical determination of chloramphenicol in food, J. Electrochem. Soc. 165 (7) (2018) B281–B288.
[63] Z. Yu, H. Li, X. Zhang, N. Liu, X. Zhang, NiO/graphene nanocomposite for determination of H_2O_2 with a low detection limit, Talanta 144 (2015) 1–5.
[64] G. Zeng, W. Li, S. Ci, J. Jia, Z. Wen, Highly dispersed NiO nanoparticles decorating graphene nanosheets for non-enzymatic glucose sensor and biofuel cell, Sci. Rep. 6 (2016) 36454.
[65] T. Kokulnathan, S. Sakthinathan, S.M. Chen, R. Karthik, T.W. Chiu, Hexammine cobalt(III) coordination complex grafted reduced graphene oxide composite for sensitive and selective electrochemical determination of morin in fruit samples, Inorg. Chem. Front. 5 (2018) 1145–1155.
[66] Q. Li, W. Gao, X. Zhang, H. Liu, M. Dou, Z. Zhang, F. Wang, Mesoporous NiO nanosphere: a sensitive strain sensor for determination of hydrogen peroxide, RSC Adv. 8 (2018) 13401–13407.
[67] W. Liu, H. Zhang, B. Yang, Z. Li, L. Lei, X. Zhang, A non-enzymatic hydrogen peroxide sensor based on vertical NiO nanosheets supported on the graphite sheet, J. Electroanal. Chem. 749 (2015) 62–67.
[68] S. Jana, S. Samai, B.C. Mitra, P. Bera, A. Mondal, Nickel oxide thin film from electrodeposited nickel sulfide thin film: peroxide sensing and photodecomposition of phenol, Dalton Trans. 43 (2014) 13096–13104.
[69] L. Lorencova, T. Bertok, J. Filip, M. Jerigova, D. Velic, P. Kasak, K.A. Mahmoud, J. Tkac, Highly stable $Ti_3C_2T_x$ (MXene)/Pt nanoparticles-modified glassy carbon electrode for H_2O_2 and small molecules sensing applications, Sens. Actuators, B 263 (2018) 360–368.